PAPER

Check for updates

Synthesis, structure and slow magnetic relaxation of lanthanoid coordination polymers based on ethynyl-bridged picolinate ligands

Verónica Jornet-Mollá, [ID] Carlos J. Gómez-García, [ID] * Miquel J. Dolz-Lozano, Carlos Giménez-Saiz [ID] and Francisco M. Romero [ID] *

A heteroditopic ligand (H$_2$**L$_1$**) containing picolinate and benzoate moieties segmented by a triple bond has been used in the preparation of a family of isostructural coordination polymers of the formula [(CH$_3$)$_2$NH$_2$][Ln((H$_2$O)$_2$**L$_1$**)$_2$] (Ln = Eu (**1**), Gd (**2**), Tb (**3**), Dy (**4**), Ho (**5**) and Er (**6**)). The single crystal structures show that these compounds crystallize in the monoclinic *I2/a* space group and form anionic layers with rhomboidal voids. AC magnetic susceptibility measurements show that compounds based on Kramers ions, such as the Gd (**2**), Dy (**4**) and Er (**6**) derivatives, present slow relaxation of magnetization (SRM) under an applied DC magnetic field. On the other hand, Tb (**3**) and Ho (**5**) compounds, based on non-Kramers ions, lack SRM properties. Compound **2** is one of the few reported Gd(III) compounds showing slow relaxation behaviour.

Introduction

Lanthanoid coordination polymers (Ln-CPs) have recently attracted a lot of interest in view of their fascinating photophysical and magnetic properties.[1–3] In comparison with transition metals, lanthanoids have higher coordination numbers and more flexible coordination geometries and, therefore, a wide variety of interesting topological networks have been reported: 1D chains,[4] 2D grids,[5] 3D porous structures[6] and interpenetrating architectures.[7] Owing to these reasons, Ln-CPs show great potential for applications in different fields, such as catalysis, adsorption, luminescent sensors and magnetic materials for molecular spintronics and quantum information technologies.[8,9] However, their coordination spheres and structures are hard to predict and the design of high-dimensional Ln-CPs remains challenging.[10]

Due to their strong ionic character and poor electron delocalization, the magnetism of lanthanoid coordination complexes had attracted less attention in the past, in comparison with transition metal ions. This changed completely after the observation of single-molecule magnetic (SMM) behaviour in the lanthanoid bis-phthalocyanine complexes, [LnPc$_2$]$^-$ (Ln = Dy, Tb; Pc = phthalocyanine), reported by Ishikawa and coworkers.[11,12] From then on, it has been clearly established that the combination of unquenched spin–orbital angular momentum and crystal-field effects can lead to very large magnetic anisotropies of some lanthanoid ions, inducing huge energy barriers for reversal of the magnetization, a typical characteristic of the SMM character.[13,14] While most cases concern Dy(III) compounds,[15] examples of other ions, such as Tb^{3+}, Er^{3+} and Ho^{3+}, are also known.[16] Many of these lanthanoid SMMs are mononuclear,[17] but examples of higher nuclearities also exist.[18–22] Ln-CPs exhibiting slow magnetic relaxation are also widely known.[15,23–27] Since the magnetic interactions between lanthanoid ions are rather weak, the slow magnetic relaxation observed in many of these extended compounds is due essentially to single ion anisotropy effects.[28]

Lanthanoid single-ion magnetic anisotropy arises from the splitting of the m_J states by the electrostatic effects of the crystal field. The energy gap between the different $\pm m_J$ doublets (which determines the energy barrier for magnetization reversal) is thus very sensitive to the coordination environment. By a judicious match of the ligand field with the shape of the electronic density of the free metal ions, the energy barrier can be greatly enhanced.[29] As proposed by Long and coworkers, an equatorial crystal field is needed to maximize the magnetic anisotropy of Er^{3+} ions, characterised by a prolate electron density. On the other hand, Dy^{3+} and Tb^{3+} having an oblate electron density would need an axial crystal field. The family of dysprosium metallocenes, with a strongly axial coordination environment, ranks among the best examples of SMM behavior.[30] Efforts are currently focused on the preparation of air-stable mononuclear lanthanoid-based SMMs with very high energy barriers for magnetization

Departament de Química Inorgànica, Universitat de València, C/Dr Moliner, 50, 46100 Burjassot, Spain. E-mail: fmrm@uv.es

Paper

reversal.[31,32] Arranging lanthanoid SMMs into coordination polymers, in which the lanthanoid coordination sphere can be constrained by the bridging linkers and the crystal symmetry, has been suggested as a valuable strategy to improve the magnetic properties of these materials.[15,33] Complexes with the same coordination environment can be assembled in the crystal lattice in different ways, providing insight into the relevance of dipolar interactions for tuning the SMM properties.[34]

Rigid benzenedicarboxylate-type ligands, for example, 5-(4-pyridyl)-isophthalic acid (H_2IP-Py), isophthalic acid (H_2IP) and terephthalic acid (H_2TP), have been widely employed in the preparation of Ln-CPs.[35] Compared with benzenedicarboxylate ligands, the use of picolinate ligands is still scarcely investigated. In fact, only one family of anionic networks prepared from 5-(4-carboxyphenyl)picolinic acid and lanthanoid ions have been reported.[36] Prompted by this lack of studies, we have undertaken the synthesis and magnetic studies of Ln-CPs based on a family of segmented rigid polypicolinate ligands.[37,38] As part of this project, we report now on a series of coordination polymers of the formula $[(CH_3)_2NH_2][Ln(H_2O)_2(L_1)_2]$ (Ln = Eu (**1**), Gd (**2**), Tb (**3**), Dy (**4**), Ho (**5**) and Er (**6**)), based on the ditopic ligand 5-((4-carboxyphenyl)ethynyl) picolinate (L_1^{2-}), featuring benzoate and picolinate subunits bridged by an ethynylene spacer (Chart 1). In a separate work, the synthesis, structural characterization and luminescence properties of the europium compound **1** have been reported.[39]

Experimental

Materials and methods

All chemicals and solvents were used as received. Ligand L_1^{2-} was synthesized as previously described.[37]

Synthesis of $[(CH_3)_2NH_2][Ln(H_2O)_2(L_1)_2]$ (Ln = Eu (1), Gd (2), Tb (3), Dy (4), Ho (5) and Er (6)). A solution of $Eu(NO_3)_3 \cdot 6H_2O$ or $LnCl_3 \cdot 6H_2O$ and 5-((4-carboxyphenyl)ethynyl)picolinic acid (2 equiv.) in DMF/H_2O (3 : 2 ratio) was placed in a glass vial and stirred for 30 min. Next, 2–3 drops of nitric acid (65%, aq.) were added and the resulting suspension was placed in an oven. The mixture was heated at 130 °C for 3 days and then cooled to room temperature at a cooling rate of 0.2 K min^{-1}. Colourless crystals were filtered and air-dried to give compounds **1–6**. Details concerning yields, elemental analyses and IR spectra are given in the SI.

Single crystal X-ray diffraction. Suitable crystals of **1–6** were coated with Paratone® N oil, fixed on a small fibre loop and mounted on an Oxford Diffraction Supernova diffractometer equipped with a graphite-monochromated Enhance Mo X-Ray Source (λ = 0.71073 Å) at 120 K. The data collection routines,

unit cell refinements and data processing were carried out using the CrysAlis software package.[40] The structures were solved using SHELXT 2018/2 via the WinGX graphical interface[41] and refined using SHELXL-2019/2.[42] All non-hydrogen atoms were refined anisotropically. H atoms on carbon atoms were included at calculated positions and refined with a riding model with relative isotropic displacement parameters. On the other hand, H atoms on solvent molecules and amine H atoms on dimethylammonium cations were found in Fourier difference maps and refined with constrained isotropic thermal parameters. CCDC 2392560–2392564 contain the supplementary crystallographic data for **2–5**, respectively. CCDC 2068840 contains the corresponding data for previously reported **1**.[39] These data are provided free of charge by The Cambridge Crystallographic Data Centre.

Powder X-ray diffraction (PXRD). PXRD measurements of compounds **1–6** were performed at room temperature using Cu Kα radiation (λ = 1.54056 Å) in a 2–40° 2θ range. Polycrystalline samples were lightly ground in an agate mortar and filled into a 0.5 mm borosilicate capillary prior to being mounted and aligned on an Empyrean PANalytical powder diffractometer. Simulated diffractograms were obtained from single crystal X-ray data using the CrystalDiffract software.

Magnetic susceptibility measurements. Variable temperature susceptibility measurements were carried out for compounds **1–6** in the temperature range of 2–300 K with an applied magnetic field of 100 mT on ground polycrystalline samples using a Quantum Design (San Diego, CA, USA) MPMS XL-5 SQUID magnetometer. The susceptibility data were corrected for the sample holder and the diamagnetic contributions of the sample, using Pascal's constants.[43] AC susceptibility measurements were performed on the same samples of compounds **2–6** at low temperatures with different applied DC fields in the frequency range of 10 Hz–10 kHz using the Quantum Design (San Diego, CA, USA) PPMS-9 equipment.

Other characterization techniques. IR transmission measurements were performed for powdered samples at room temperature using an FT-IR spectrometer (Bruker, Alpha II) equipped with an attenuated total reflection (ATR) accessory in the range of 400–4000 cm^{-1}. C, H and N elemental analyses were performed using a CE INSTRUMENTS 1110 EA elemental analyzer (SCSIE, Universitat de València). Thermogravimetric analyses were performed on Mettler-Toledo TGA/SDTA/851e apparatus under an N_2 atmosphere at a scan rate of 10 K min^{-1}.

Results and discussion

Synthesis and characterization

Crystalline lanthanoid(III) coordination polymers **1–6** were prepared by the reaction of lanthanoid(III) chlorides (or nitrates) with the picolinic acid ligand H_2L_1 at a high temperature. The addition of an acid modulator (nitric acid) was necessary in order to obtain single crystals suitable for structural characterization. All the compounds could also be obtained from the corresponding methyl diester under similar conditions.
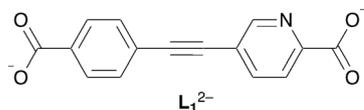

Chart 1 The segmented picolinate-based ligand used in this work.

The phase purity of the bulk materials was confirmed by PXRD measurements. The experimental diffractograms recorded at room temperature for compounds **1–6** (Fig. S1) match perfectly the simulated patterns obtained from single crystal data of the Tb derivatives at 120 K, indicating that all the compounds in the series are isostructural.

Thermogravimetric (TG) analyses were performed under a nitrogen atmosphere (Fig. S2). TG curves for **1–6** are very similar and present three separate steps of weight loss. The first one corresponds to around 5% of total weight and takes place between 416 and 435 K. It is ascribed to the release of two coordinated water molecules (calcd: 4.71–4.62%). The second and third steps occur above 550 K and are attributed to the decomposition of dimethylammonium cations and L_1^{2-} ligands, respectively. These results are consistent with the formulation deduced from single crystal X-ray diffraction measurements, which shows the presence of two water molecules per lanthanoid ion.

Structural properties

An analysis of single crystal X-ray data shows that **1–6** are isostructural (Table 1) and crystallize in the monoclinic space group $I2/a$. Their asymmetric units contain half Ln^{3+} cation and half $[(CH_3)_2NH_2]^+$ cation, both sitting on a twofold axis, one L_1^{2-} dianion and one coordinated water molecule. The alkylammonium cation compensates the negative charge of

the host framework and originates from the hydrolysis of dimethylformamide (DMF) solvent molecules.[44,45]

The lanthanoid cation exhibits an octacoordinated distorted square antiprism geometry (Fig. 1). It is surrounded by two chelating picolinate subunits with Ln–O3 distances in the 2.36–2.42 Å range, considerably shorter than the Ln–N1 distances, lying between 2.52 and 2.59 Å (Table S1). This is expected from the strong oxophilicity of the Ln^{3+} cations.[36] Two water molecules (with Ln–O1W distances between 2.31 and 2.38 Å) and two monodentate benzoate groups with slightly shorter bonds (Ln–O1: 2.30–2.35 Å) complete the coordination sphere of the lanthanoid ions. The water molecules and benzoate anions coordinating to the same Ln^{3+}
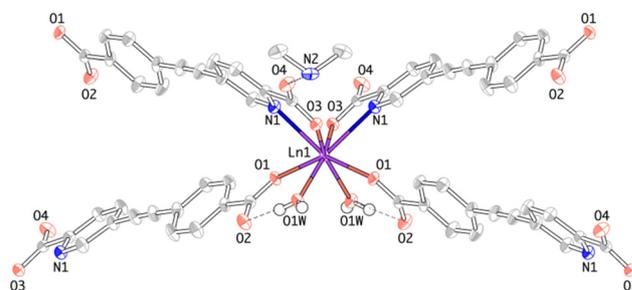

Fig. 1 Thermal ellipsoid plot of the Ln^{3+} coordination environment in **1–6**.

Table 1 Crystallographic data

	1[b]	**2**	**3**	**4**	**5**	**6**
Chemical formula	$C_{32}H_{26}EuN_3O_{10}$	$C_{32}H_{26}GdN_3O_{10}$	$C_{32}H_{26}TbN_3O_{10}$	$C_{32}H_{26}DyN_3O_{10}$	$C_{32}H_{26}HoN_3O_{10}$	$C_{32}H_{26}ErN_3O_{10}$
a (Å)	11.97630(10)	11.9735(2)	11.95379(12)	11.93791(9)	11.9306(2)	11.93381(13)
b (Å)	10.67410(10)	10.7027(2)	10.71643(11)	10.73099(12)	10.7799(2)	10.72771(15)
c (Å)	24.7299(3)	24.6745(4)	24.5755(3)	24.5071(3)	24.3559(4)	24.4262(3)
α (°)	90.00	90.00	90.00	90.00	90.00	90.00
β (°)	98.0830(10)	98.214(2)	98.3607(9)	98.3972(8)	98.763(2)	98.6388(11)
γ (°)	90.00	90.00	90.00	90.00	90.00	90.00
V (Å^3)	3129.97(6)	3129.57(9)	3114.71(6)	3105.84(6)	3095.86(9)	3091.62(7)
T (K)	120.2(3)	119.9(3)	119.9(3)	119.95(10)	119.9(3)	120.00(10)
Z	4	4	4	4	4	4
M_r (g mol^{-1})	764.52	769.81	771.48	775.06	777.49	779.82
Crystal system	Monoclinic	Monoclinic	Monoclinic	Monoclinic	Monoclinic	Monoclinic
Space group	$I2/a$ (No. 15)	$I2/a$ (No. 15)	$I2/a$ (No. 15)	$I2/a$ (No. 15)	$I2/a$ (No. 15)	$I2/a$ (No. 15)
Crystal dimensions (mm)	0.224 × 0.151 × 0.104	0.390 × 0.281 × 0.150	0.324 × 0.194 × 0.118	0.336 × 0.154 × 0.085	0.121 × 0.105 × 0.083	0.340 × 0.203 × 0.106
μ(Mo Kα) (mm^{-1})	2.066	2.182	2.333	2.469	2.619	2.778
λ (Å)	0.71073	0.71073	0.71073	0.71073	0.71073	0.71073
Density (Mg m^{-3})	1.622	1.634	1.645	1.658	1.668	1.675
Index ranges for h, k, l	−16/16, −14/14, −34/34	−14/15, −13/14, −31/32	−15/15, −14/14, −32/31	−15/15, −13/13, −31/30	−15/15, −14/13, −30/31	−16/16, −13/14, −33/33
2θ range (°)	6.378–59.506	6.674–55.256	6.704–55.480	6.404–55.552	6.770–55.474	6.748–59.642
Goodness-of-fit on F^2	1.153	1.111	1.097	1.119	1.098	1.085
Reflns collected	37 152	26 278	40 403	58 070	28 834	36 543
Independent reflns (R_{int})	4273 (0.0249)	3421 (0.0251)	3519 (0.0244)	3495 (0.0364)	3413 (0.0517)	4193 (0.0300)
Data/restraints/parameters	4273/0/218	3421/0/218	3519/0/218	3495/0/218	3413/0/218	4193/0/218
$R1$, w$R2$ [$I > 2\sigma(I)$][a]	0.0145, 0.0355	0.0143, 0.0365	0.0128, 0.0311	0.0159, 0.0358	0.0257, 0.0494	0.0149, 0.0354
$R1$, w$R2$ (all data)[a]	0.0158, 0.0363	0.0153, 0.0371	0.0140, 0.0318	0.0184, 0.0375	0.0317, 0.0522	0.0167, 0.0364

[a] $R1 = \sum(|F_o| - |F_c|)/\sum|F_o|$; w$R2 = [\sum[w(F_o^2 - F_c^2)^2]/\sum[wF_o^4]]^{1/2}$. [b] Published in a separate work.[39]

cation form a very strong *intramolecular* H-bond (average distance: O1W⋯O2: 2.587 ± 0.011 Å).

Continuous shape measure (CShM) calculations using SHAPE 2.1 confirm that the coordination geometries of **1–6** are distorted square antiprisms (with minimum CShM calculated values corresponding to a D_{4d} symmetry, Table S2).[46–49] In compounds **1–6**, an average value of 9.133 suggests an important distortion from the ideal geometry. In fact, the skew angles (Φ), described as the offset between the two squares defined by the mean planes through the coordinated atoms, lie between 49.5° (Eu) and 48.6° (Ho), differing from the value expected for an ideal D_{4d} symmetry ($\Phi = 45°$).

The heteroditopic ligand $\mathbf{L_1}^{2-}$ connects two Ln^{3+} cations by involving the two coordinating subunits (chelating picolinate and monodentate benzoate anions). In turn, each Ln^{3+} cation is surrounded by four $\mathbf{L_1}^{2-}$ ligands. This connectivity results in the formation of a 2D rhombus grid layer that presents channels (average size: 7.36 × 20.56 Å) along the *a* axis (Fig. S3). Dimethylammonium cations sit into these voids (one cation per channel) and are connected to the host structure by hydrogen bonds (Table S3) with the non-coordinated picolinate oxygen atoms (average distance N2⋯O4: 2.723 ± 0.005 Å).

Additional hydrogen bonds (Table S3) between coordinated water molecules and picolinate oxygen atoms (average distance: O1W⋯O3: 2.776 ± 0.010 Å) connect complexes of consecutive layers related by the centre of symmetry, bringing the lanthanoid cations to a relatively short distance lying between 6.133 Å (Eu) and 6.113 Å (Ho). This leads to a three-dimensional H-bonded network with an alternating AA′AA′ arrangement (Fig. 2). Furthermore, π–π stacking interactions involve pyridine and benzene aromatic rings of adjacent layers.

In all the compounds, the ligand $\mathbf{L_1}^{2-}$ shows a nearly planar conformation (Table S4), with small dihedral angles between the pyridine and benzene rings (mean value: 12.9 ± 0.8°). Furthermore, the picolinate fragment exhibits a low torsion angle (mean value: 6.8 ± 0.9°) and the geometry of the triple bond is almost linear (average –C–C–C– bond angles of 177.9 ± 0.8° and 177.5 ± 0.6°).

A family of lanthanoid complexes based on a similar heteroditopic ligand 5-(4-carboxyphenyl)picolinate dianion (CPA^{2-}) has been reported.[36] The resulting compounds of the formula $[(CH_3)_2NH_2][Ln(H_2O)_2(CPA)_2]$ are isostructural to **1–6**, although the crystal structure of these compounds was initially reported in the $C2/c$ space group, due to the choice of a non-conventional unit cell.[50] The lanthanoid coordination sphere is analogous to that described for **1–6**, and identical rhombus grid layers are formed. Owing to the presence of the ethynylene spacer, the size of the channels in **1–6** along its longest direction is notably higher in comparison with this family of compounds. Moreover, it is worth noting that the channels present a hydrophilic character, due to the fact that they are internally covered by non-coordinated carboxylate oxygen atoms that may allow specific interactions between guest molecules and the host framework in post-synthetic cation exchange processes. These post-synthetic processes allow the fabrication of new materials with enhanced properties that
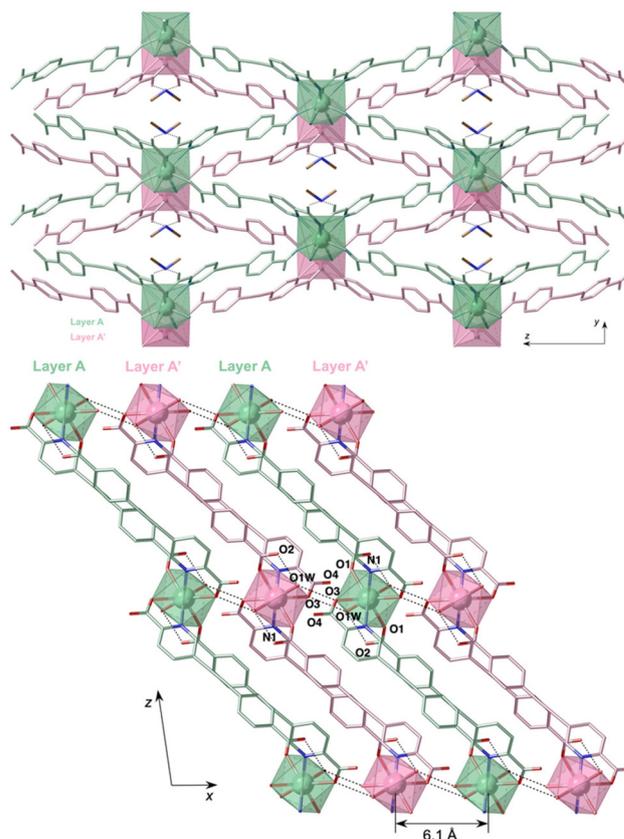

Fig. 2 View of the crystal structure of **1–6** along the *x* (top) and *y* (bottom) directions showing the layered structure. H atoms have been omitted for clarity.

may not be possible to obtain by direct methods. For instance, the replacement of dimethylammonium cations with Li^+ ions in $[(NH_2)(CH_3)_2]_2[Zn_2(BDC)_3(DMA)_2]\cdot 6DMF$ (BDC^{2-} = 1,4-benzenedicarboxylate; DMA = dimethylamine) results in an increase in its internal surface area and methane sorption capacity.[51] In another case, exchange of the nickel(II) cations located in the pores of $Ni_2[Ni_4[Cu_2\text{-}(Me_3mpba)_2]_3]\cdot 54H_2O$ (Me_3mpba^{4-} = *N,N′*-2,4,6-trimethyl-1,3-phenylenebis(oxamate) ligand) with barium cations produces a novel coordination polymer that presents improved features for SO_2 adsorption.[52]

Lanthanoid chemistry generally results in the formation of isostructural compounds since lanthanoid ions exhibit common chemical properties. Nevertheless, lanthanoid contraction can lead to slight structural changes or result in full structural rearrangements that influence the physical properties of the materials. In the latter scenario, the structure of the polymers varies dramatically with increasing atomic number of the lanthanoid ion. For instance, the complexes $[Ln_2(HL)_3(H_2O)_n]\cdot XH_2O$ (HL^{2-} = 3,5-pyrazoledicarboxylate) range from porous 3D frameworks (Ln = La–Pr, Nd and Sm) and 2D double decker structures (Ln = Eu, Gd and Tb) to 2D monolayer frameworks (Ln = Dy, Ho and Er).[53] In our case, all the compounds **1–6** are isostructural but it can be seen that, with increasing atomic number, the cell volume and Ln–O and
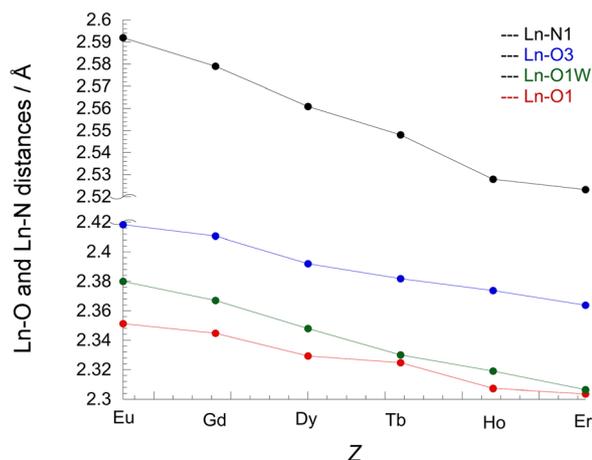
Fig. 3 Variation of the Ln−ligand bond lengths with increasing atomic number (Z) of lanthanoid ions for **1−6**.

Ln–N bond lengths decrease continuously. The same is observed for intramolecular and cation–anion H-bonding interactions (Table S3). This is a clear signature of the *lanthanoid contraction effect* (Fig. 3). The dimensions of the channels exhibit continuous variation across the lanthanoid series: the long dimension becomes shorter with increasing atomic number, whereas the short dimension shows quite the opposite effect (Table S5). With respect to the ligand geometry, deviation from coplanarity is slightly more pronounced as the cation size decreases (Table S4). This effect might be responsible for the increase of the H-bonding interaction (O1W···O3) between layers.

Magnetic properties

The thermal variation of the $\chi_m T$ product (χ_m is the molar magnetic susceptibility, Fig. 4) shows constant values at high temperatures, in agreement with those expected for the Ln^{3+} ions in their ground states (Table 2).[54] In the Eu^{3+} derivative
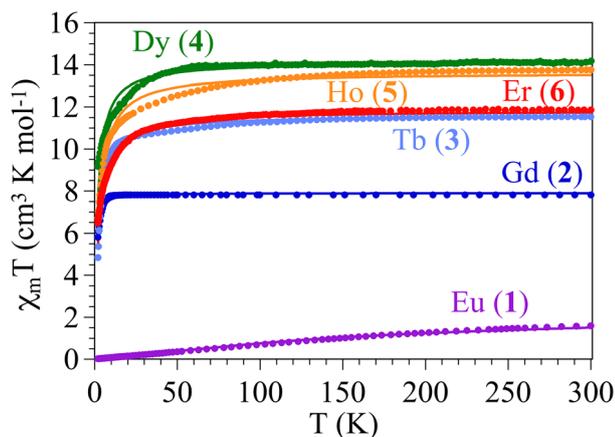

Fig. 4 Thermal variation in the $\chi_m T$ product for compounds **1−6**. Solid lines are the fits to a simple model with weak intermolecular interactions (see the text).

Table 2 DC magnetic susceptibility data for **1−6**

	1	2	3	4	5	6
Ln^{3+}	Eu^{3+}	Gd^{3+}	Tb^{3+}	Dy^{3+}	Ho^{3+}	Er^{3+}
GM^a	$^7F_0$	$^8S_{7/2}$	$^7F_6$	$^6H_{15/2}$	$^5I_8$	$^4I_{15/2}$
$g_J{}^b$	0	2	3/2	4/3	5/4	6/5
$\chi T_{calc}{}^c$	0	7.87	11.81	14.17	14.06	11.48
$\chi T_{exp}{}^d$	1.55	7.82	11.49	14.10	13.74	11.78
$g_{J\ exp}$		2.00	1.49	1.33	1.23	1.22
$\|D\|^e$ (cm^{-1})		0.93	1.18	1.39	1.15	1.48
zj^f (cm^{-1})		−0.009	−0.047	−0.034	−0.051	−0.053

^{a} GM = ground multiplet. $^b g_J = \dfrac{3}{2} + \dfrac{S(S+1) - L(L+1)}{2J(J+1)}$. $^c \chi T_{calc} = \dfrac{N_A\mu_B{}^2}{3k} g_J{}^2 J(J+1)$ (emu K mol^{-1}). ^{d} Value measured at 300 K (emu K mol^{-1}). ^{e} D: zero-field splitting parameter. ^{f} zj: mean-field parameter.

(**1**), the expected $\chi_m T$ value is zero since it has a diamagnetic $^7F_0$ ground state. Nevertheless, a room temperature value of *ca.* 1.55 cm^3 K mol^{-1} was observed (Table 2 and Fig. 4) due to thermal population of the first two excited $^7F_1$ and $^7F_2$ multiplet levels that arise from the splitting of the ground ^7F term by first-order spin–orbit coupling. As expected, when the temperature is decreased, $\chi_m T$ in compound **1** decreases due to thermal depopulation of the lowest excited multiplets and tends to zero at very low temperatures. Accordingly, we have fitted the $\chi_m T$ product of **1** to a simple expression depending only on the first-order spin–orbit coupling (λ) parameter:[55]

$$\chi_m T = \frac{N\beta^2}{3kTx} \frac{24 + Ae^{-x} + Be^{-3x} + Ce^{-6x} + De^{-10x} + Ee^{-15x} + Fe^{-21x}}{1 + 3e^{-x} + 5e^{-3x} + 7e^{-6x} + 9e^{-10x} + 11e^{-15x} + 13e^{-21x}}$$

where $A = (27x − 3)/2$, $B = (135x − 5)/2$, $C = (378x − 7)/2$, $D = (810x − 9)/2$, $E = (1485x − 11)/2$, $F = (2457x − 13)/2$ and $x = \lambda/kT$.

The best fit to this equation for compound **1** is obtained for $\lambda = 395(3)$ cm^{-1}, a value similar to those obtained for other Eu(III) complexes.[55–57]

The Gd(III) compound (**2**) shows, as expected, a constant value of around 7.8 cm^3 K mol^{-1} in the temperature range of 300–10 K and a sharp decrease at lower temperatures to reach a value of 5.7 cm^3 K mol^{-1} at 2 K (Fig. 4). This behaviour suggests the presence of a very weak antiferromagnetic coupling mediated by the carboxylate bridges. The other compounds (**3–6**) show a gradual decrease in the $\chi_m T$ value with decreasing temperature which can be attributed to the progressive depopulation of the sublevels arising from the splitting of the ground term by the presence of the ligand field and to very weak antiferromagnetic Ln–Ln interactions.[58] The magnetic properties of compounds **2–6** (solid lines in Fig. 4) were fitted with a simple model including a zero-field splitting (*D*) and an antiferromagnetic coupling (*zj*) term, using the program PHI.[59] The use of the mean-field approximation is justified since Ln–Ln interactions are very weak (Table 2) in all cases, as expected for Ln^{3+} cations connected through carboxylate bridges.[58]

Alternating current (AC) magnetic susceptibility measurements of **2–6** were performed in order to study the low-temperature magnetic relaxation behaviour of these compounds (in the presence of an oscillating AC field of 3.95 Oe). The two prerequisites for observing slow relaxation of magnetization are (i) a bistable electronic ground state, which arises from the combination of spin–orbit coupling and crystal-field splitting in the case of lanthanoid complexes, and (ii) magnetic anisotropy, being inherent in lanthanoid cations. Tb^{3+}, Dy^{3+} and Ho^{3+} exhibit oblate 4f charge distributions, whereas the distribution of Er^{3+} is prolate and that of Gd^{3+} is spherical.[29] The europium derivative was not included in these experiments due to the presence of a non-magnetic ground state. Under a zero direct current field, none of the compounds show any noticeable out-of-phase AC (χ''_m) signal, indicating a small energy barrier for spin reversal and/or fast quantum tunnelling of the magnetization.

When a DC field is applied, compounds **2** (Gd), **4** (Dy) and **6** (Er) exhibit frequency-dependent out-of-phase signals (χ''_m) (Fig. S4–S6), indicating that fast relaxation is suppressed in a DC field. In these three cases, the frequency dependence of the χ''_m signal suggests the presence of two maxima, indicating two different relaxation processes: a slow relaxation process, with a relaxation time τ_1, operating at lower frequencies and a faster relaxation process, with a relaxation time τ_2, operating at higher frequencies. This seems to be in contradiction with the existence of only one crystallographically independent Ln^{3+} ion in compounds **2–6**. However, the observation of two different relaxation processes is rather common in lanthanoid-based lattices and may be attributed to the presence of relaxation pathways *via* excited states.[60] For the Gd compound (**2**), the two maxima are clearly seen at high fields (Fig. S4). The χ''_m signal increases as the DC field is increased and the fast relaxing component reaches a maximum intensity at a static field around 120 mT. For the Dy derivative (**4**), the slow relaxation process appears below the frequency range of the experiment (Fig. S5), but it is clearly observed that the maximum of the fast relaxation process (τ_2) shifts to lower frequencies and increases its intensity with increasing magnetic field, reaching a minimum frequency and a maximum intensity for DC fields around 50 mT. For the Er derivative (**6**), the maximum of the fast relaxation process (τ_2) remains almost constant as the DC field is increased in the range of 0–60 mT and shifts to higher frequencies for higher fields (Fig. S6), reaching the highest intensity in the out-of-phase signal for H_{DC} = 80 mT.

The fit of the frequency dependence of χ''_m to a Debye model for two relaxation processes (eqn (1), solid lines in Fig. S4–S6) gives us the relaxation times (τ) for each applied DC field.[60] Despite that there are seven adjustable parameters in eqn (1), the isothermal (χ_{T1} and χ_{T2}) and adiabatic (χ_S) susceptibilities, as well as the relaxation times (τ_1 and τ_2), can be easily estimated from the in-phase signal (χ'_m) values at different frequencies and from the position of the low- and high-frequency maxima, respectively. The calculated τ_1 values are reliable only for **2** (Gd), since the maxima of the first relax-

ation process lie outside the measured frequency range for the other compounds.

$$\chi''(\omega) = (\chi_{T1} - \chi_S)\frac{(\omega\tau_1)^{1-\alpha_1}\cos\left(\frac{\pi\alpha_1}{2}\right)}{1 + 2(\omega\tau_1)^{1-\alpha_1}\sin\left(\frac{\pi\alpha_1}{2}\right) + (\omega\tau_1)^{2-2\alpha_1}}$$
$$+ (\chi_{T2} - \chi_{T1})\frac{(\omega\tau_2)^{1-\alpha_2}\cos\left(\frac{\pi\alpha_2}{2}\right)}{1 + 2(\omega\tau_2)^{1-\alpha_2}\sin\left(\frac{\pi\alpha_2}{2}\right) + (\omega\tau_2)^{2-2\alpha_2}}.$$
(1)

The relaxation times (τ_1) obtained from the fit to the Debye model increase as the DC field increases for the Gd compound but reach maxima for τ_2 at around 100 mT (Fig. S7) and 50 mT for the Dy and Er derivatives (Fig. S8 and S9). This behaviour can be well reproduced with the general model (eqn (2)),[61] with the parameters displayed in Table S6 (solid lines in Fig. S7–S9).

$$\tau^{-1} = AH^nT + \frac{B_1}{1 + B_2H^2} + D$$
(2)

A, B_1, B_2 and D in this equation are parameters corresponding to the different relaxation mechanisms: direct (A), quantum tunnelling (B_1 and B_2), Raman and Orbach (D, since they are field-independent). H is the applied DC magnetic field and n is equal to 4 for Kramers ions (Gd, Dy and Er).

Once the optimal DC fields are determined where the χ''_m signal is more intense and appears at a lower frequency (maxima in the τ_2 *vs.* H plots), a detailed study of the frequency dependence of the AC signal as a function of the temperature was performed under applied DC fields of 120, 50 and 80 mT for the Tb, Dy and Er derivatives, respectively. For the Gd derivative (**2**), the frequency dependence of χ''_m in an applied DC field of 120 mT shows at 1.9 K a maximum at around 800 Hz and a shoulder located at *ca.* 20 Hz. Both features shift to higher frequencies as the temperature increases (Fig. 5a). The fit of this data to the Debye model for two relaxation processes (eqn (1)) gives us the relaxation times τ_1 and τ_2 at each temperature. These data, displayed in an Arrhenius plot (ln τ *versus* $1/T$, Fig. 5b), show for **2** a linear dependence at high temperatures with a clear curvature at lower temperatures.[62] Attempts to fit the Arrhenius plots of compound **2** to all the possible mechanisms in eqn (3) show that the best fit is obtained including only the Orbach and direct mechanisms (second and fourth terms in eqn (3)) with the parameters displayed in Table 3 (solid lines in Fig. 5b).

$$\tau^{-1} = \tau_{QT}^{-1} + \tau_0^{-1}\exp\left(-\frac{U_{eff}}{kT}\right) + CT^n + AH^4T$$
(3)

In the case of the Dy derivative (**4**), we have studied the frequency dependence of the out-of-phase signal in a 50 mT DC field at different temperatures. At 1.9 K, we observe a maximum in the χ''_m signal at 6000 Hz (Fig. 6a). This maximum shifts continuously to higher frequencies as the temperature is increased. This behaviour indicates that the predominant mechanism for the relaxation of the magnetiza-
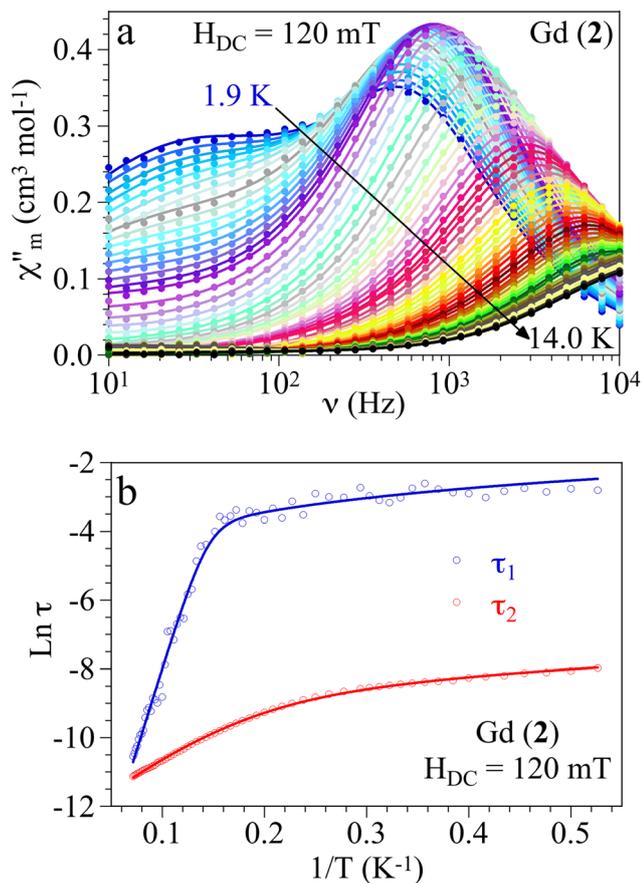
Fig. 5 (a) Frequency dependence of χ''_m for the Gd derivative (**2**) in a DC field of 120 mT at different temperatures. Solid lines are the best fit to the Debye model for two processes (eqn (1)). (b) Arrhenius plot of the relaxation times for **2** in a DC field of 120 mT. The solid line is the best fit to a model with direct and Orbach relaxation mechanisms (eqn (3)).

Fig. 6 (a) Frequency dependence of χ''_m for the Dy derivative (**4**) in a DC field of 50 mT at different temperatures. Solid lines are the best fit to the Debye model for two processes (eqn (1)). (b) Arrhenius plot of the relaxation times for **2** in a DC field of 50 mT. The solid line is the best fit to a model with direct and Orbach relaxation mechanisms (eqn (3)).

tion is thermally activated. We have fitted the data to a Debye model for two relaxation processes (eqn (1)) to obtain the relaxation times of the fast relaxation process (τ_2) at each temperature (τ_1 values are unreliable, the slow relaxation process lying outside the frequency range). The Arrhenius plot (ln τ versus 1/T, Fig. 6b) shows a linear behaviour with a very slight curvature at low temperatures, pointing to the presence of a thermally activated mechanism. Attempts to fit the data with the three possible mechanisms (quantum tunnelling was discarded in the presence of an applied DC field) show that the data can be fitted to Orbach and direct mechanisms with the parameters shown in Table 3 (solid line in Fig. 6b).
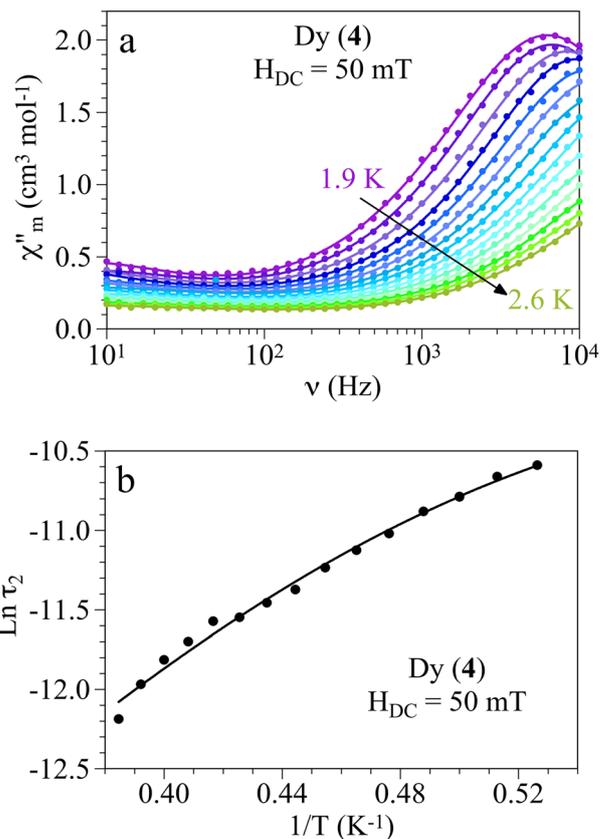
A similar study was performed for the Er compound (**6**). In this case, the DC field was set to 80 mT and the frequency dependence of the out-of-phase signal was measured at low temperatures in the 1.9–2.35 K range (Fig. 7a). Fitting of the data to a Debye model for two relaxation processes (eqn (1)) yields the relaxation times of the fast relaxation process (τ_2) at each temperature (τ_1 values are again unreliable). The Arrhenius plot (ln τ versus 1/T, Fig. 7b) also shows a linear behaviour with a very slight curvature at low temperatures. As in the case of **4**, the data can be fitted to Orbach and direct mechanisms with the parameters shown in Table 3 (solid line in Fig. 7b).

It is worth noting that **2** is one of the few reported Gd(III) lattices showing slow relaxation of magnetization (SRM). In

Table 3 Magnetic parameters obtained from the fit of the Arrhenius plot to the general model (eqn (3))

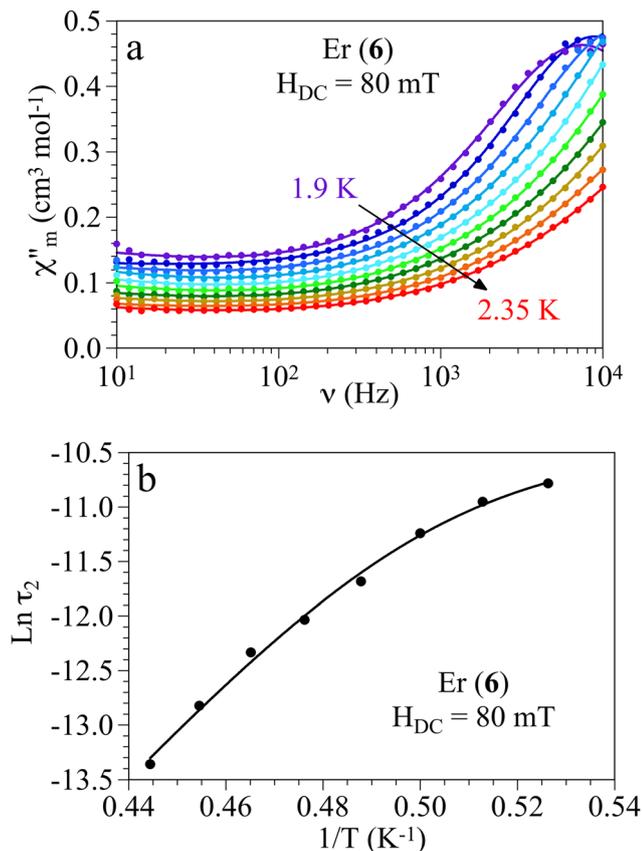| Compound	H_{DC} (mT)	Process	AH^4 (K^{-1})	τ_0 (s)	U_{eff} (K)
2 (Gd)	120	τ_1	6.3(3)	$2.5(6) \times 10^{-9}$	95(3)
		τ_2	$1.51(1) \times 10^3$	$4.4(1) \times 10^{-6}$	21.4(3)
4 (Dy)	50	τ_2	$1.4(3) \times 10^4$	$1.1(8) \times 10^{-8}$	17(2)
6 (Er)	80	τ_2	$1.9(2) \times 10^4$	$1.1(2) \times 10^{-15}$	48(3)

Fig. 7 (a) Frequency dependence of χ''_m for the Er derivative (**6**) in a DC field of 80 mT at different temperatures. Solid lines are the best fit to the Debye model for two processes (eqn (1)). (b) Arrhenius plot of the relaxation times for **6** in a DC field of 80 mT. The solid line is the best fit to a model with direct and Orbach relaxation mechanisms (eqn (3)).

comparison with the many reported Dy(III) compounds showing SRM,[63–66] the number of Gd(III) compounds showing SRM is much lower. Since the Gd^{3+} ion has a half-filled $4f^7$ configuration, the ground state multiplet $^8S_{7/2}$ is magnetically isotropic, excluding in principle the existence of an energy barrier for spin reorientation. Thus, it has been suggested that slow relaxation in Gd(III) complexes can be ascribed to a phonon-bottleneck effect.[67] This picture assumes that the wavelength of the resonant phonon is larger than the separation between Gd^{3+} ions, a situation that could be possible in **2**, where the lanthanoid cations are separated by a distance slightly larger than 6 Å. However, although the first reports on SRM of Gd(III) compounds refer to polymeric structures containing short Gd–Gd distances,[28,68–70] well isolated mononuclear Gd(III) compounds exhibiting SRM have been reported.[71] It has been argued that zero-field splitting in strongly distorted environments could account for the efficiency of the resonant phonon trapping.[72]

Finally, the AC magnetic susceptibility of **3** (Tb) and **5** (Ho) shows that these compounds lack SRM properties, even in the presence of a DC magnetic field. This may be related to the fact that Tb^{3+} and Ho^{3+} are non-Kramers ions. In fact, previous

studies show that a strong axial crystal-field symmetry is needed for the observation of SRM effects in non-Kramers ions. In the case of compounds **1–6**, there are four shortest Ln–O distances leading to an equatorial-like ligand field that may induce a larger energy barrier for spin reorientation in the erbium(III) compound.

Conclusions

A heteroditopic ligand L_1^{2-} containing distant picolinate and benzoate anions connected by an ethynylene bridge has been used in the synthesis of a family of 2D anionic coordination lattices of the formula $[(CH_3)_2NH_2][Ln(H_2O)_2(L_1)_2]$ (Ln = Eu (**1**), Gd (**2**), Tb (**3**), Dy (**4**), Ho (**5**) and Er (**6**)). AC magnetic measurements show that lanthanoid ions with doubly degenerate ground states (Kramers doublets) **2**, **4** and **6** present slow relaxation of magnetization when a DC magnetic field is applied. It has been shown that, under these conditions, the dynamic properties of these compounds follow direct and Orbach mechanisms. On the other hand, non-Kramers ions (**3** and **5**) show lack of slow dynamic properties. Interestingly, compound **2** constitutes one of the few examples of slow relaxation in a Gd(III) compound.

Author contributions

Conceptualization, F. M. R.; formal analysis, V. J. M., C. J. G. G., M. J. D. L., C. G. S. and F. M. R.; investigation, V. J. M., C. J. G. G. and F. M. R.; writing – original draft preparation, C. J. G. G. and F. M. R.; and writing – review and editing, V. J. M., C. J. G. G., M. J. D. L., C. G. S. and F. M. R. All authors have read and agreed to publish this version of the manuscript.

Conflicts of interest

There are no conflicts to declare.

Data availability

The data supporting this article have been included as part of the SI.

Supplementary Information contains experimental details of the synthesis and characterization of **1–6**. Table S1: Bond distances (Å) defining the coordination sphere of **1–6**; Table S2: Continuous shape measures (CShM) for **1–6** using SHAPE 2.1; Table S3: Relevant hydrogen bond distances (Å) in the crystal structures of compounds **1–6**; Table S4: Relevant intraligand angles (deg) in the crystal structures of compounds **1–6**; Table S5: Dimensions (Å) of apparent channels in the crystal structures of compounds **1–6**; Table S6: Magnetic parameters obtained from the fit of the field dependence of the relaxation times at 1.9 K (eqn 2); Table S7: Magnetic para-

meters obtained from the fit of the Arrhenius plot to the general model (equation 4); Fig. S1: Comparison of the powder X-ray diffractograms of **1–6** with the simulation obtained from the corresponding single crystal X-ray data for 3 using CrystalDiffract software (shown in black); Fig. S2: Thermogravimetric analysis of **1–6** under a nitrogen atmosphere; Fig. S3. Representation of the layered structure of **1–6** in the yz plane; Fig. S4. Frequency dependence of the out-of-phase susceptibility (χ''_m) for the Gd derivative (**2**) at 1.9 K in different applied DC fields. Solid lines are the best fit to the Debye model for two processes (eqn 1); Fig. S5: Frequency dependence of the out-of-phase susceptibility (χ''_m) for the Dy derivative (**4**) at 1.9 K in different applied DC fields. Solid lines are the best fit to the Debye model for two processes (eqn 1); Fig. S6: Frequency dependence of the out-of-phase susceptibility (χ''_m) for the Er derivative (**2**) at 1.9 K in different applied DC fields. Solid lines are the best fit to the Debye model for two processes (equation 1); Fig. S7: Field dependence of the relaxation time of both relaxation processes in the Gd derivative (**2**) at 1.9 K. Solid line is the fit to the model (see text); Fig. S8. Field dependence of the relaxation time of the fast relaxation process (τ_2) in the Dy derivative (**4**) at 1.9 K. Solid line is the fit to the model (see text); Fig. S9. Field dependence of the relaxation time of the fast relaxation process (τ_2) in the Er derivative (**6**) at 1.9 K. Solid line is the fit to the model (see text). See DOI: https://doi.org/10.1039/d5dt01330e.

CCDC 2392560–2392564 contain the supplementary crystallographic data for this paper.[73a–e]

Acknowledgements

References

1 H.-Q. Yin and X.-B. Yin, Metal–organic frameworks with multiple luminescence emissions: designs and applications, *Acc. Chem. Res.*, 2020, **53**, 485–495.

2 C. Blais, G. Calvez, Y. Suffren, C. Daiguebonne, C. Paranthoen, E. Bazin, S. Freslon, K. Bernot and O. Guillou, Luminance and brightness: application to lanthanide-based coordination polymers, *Inorg. Chem.*, 2022, **61**, 19588–19596.

3 P. Konieczny, W. Sas, D. Czernia, A. Pacanowska, M. Fitta and R. Pelka, Magnetic cooling: a molecular perspective, *Dalton Trans.*, 2022, **51**, 12762–12780.

4 M.-Y. Ye, M.-X. Zhang, Q.-F. Xu, H. Xu, L.-S. Long and L.-S. Zheng, Highly stable Eu-coordination polymer exhibiting the highest quantum yield, *Sci. China: Chem.*, 2023, **66**, 1400–1405.

5 Z.-Y. Li, Y.-Q. Cao, J.-Y. Li, X.-F. Zhang, B. Zhai, C. Zhang, F.-L. Zhang and G.-X. Cao, Three types of lanthanide coordination polymers with methylmalonate and isonicotinate as coligands: structures, luminescence, and magnetic properties, *Cryst. Growth Des.*, 2017, **17**, 6752–6761.

6 L.-X. You, S.-Y. Xie, C.-C. Xia, S.-J. Wang, G. Xiong, Y.-K. He, I. Dragutan, V. Dragutan, V. Fedin and Y.-G. Sun, Unprecedented homochiral 3D lanthanide coordination polymers with triple-stranded helical architecture constructed from a rigid achiral aryldicarboxylate ligand, *CrystEngComm*, 2019, **21**, 1758–1763.

7 A. B. Ruiz-Muelle, A. García- García, A. A. García-Valdivia, I. Oyarzabal, J. Cepeda, J. M. Seco, E. Colacio, A. Rodríguez-Diéguez and I. Fernández, Design and synthesis of a family of 1D-lanthanide-coordination polymers showing luminescence and slow relaxation of the magnetization, *Dalton Trans.*, 2018, **47**, 12783–12794.

8 L. Bogani and W. Wernsdorfer, Molecular spintronics using single-molecule magnets, *Nat. Mater.*, 2008, **7**, 179.

9 D. W. Laorenza and D. E. Freedman, Could the quantum internet be comprised of molecular spins with tunable optical interfaces?, *J. Am. Chem. Soc.*, 2022, **144**, 21810–21825.

10 B. Zhang, Z. Cheng, Y. Wu, L. Chen, R. Jing, X. Cai, C. Jiang, Y.-Q. Zhang, A. Yuan, H.-H. Cui and Z.-Y. Li, Pseudo-mono-axial ligand fields that support high energy barriers in triangular dodecahedral Dy(III) single-ion magnets, *Chem. Sci.*, 2022, **13**, 13231–13240.

11 N. Ishikawa, M. Sugita, T. Ishikawa, S. Koshihara and Y. Kaizu, Lanthanide double-decker complexes functioning as magnets at the single-molecular level, *J. Am. Chem. Soc.*, 2003, **125**, 8694–8695.

12 N. Ishikawa, M. Sugita, T. Ishikawa, S. Koshihara and Y. Kaizu, Mononuclear lanthanide complexes with a long magnetization relaxation time at high temperatures: A new category of magnets at the single-molecular level, *J. Phys. Chem. B*, 2004, **108**, 11265–11271.

13 F.-S. Guo, A. K. Bar and R. A. Layfield, Main group chemistry at the interface with molecular magnetism, *Chem. Rev.*, 2019, **119**, 8479–8505.

14 K. Bernot, Get under the umbrella: a comprehensive gateway for researchers on lanthanide–based single–molecule magnets, *Eur. J. Inorg. Chem.*, 2023, **26**, e202300336.

15 Q. Wan, M. Wakizaka and M. Yamashita, Single-ion magnetism behaviors in lanthanide (III) based coordination frameworks, *Inorg. Chem. Front.*, 2023, **10**, 5212–5224.

16 K. R. Meihaus and J. R. Long, Magnetic blocking at 10 K and a dipolar-mediated avalanche in salts of the bis((η^8-

cyclooctatetraenide) complex $[Er(COT)_2]^-$, *J. Am. Chem. Soc.*, 2013, **135**, 17952–17957.

17 M. A. AlDamen, S. Cardona-Serra, J. M. Clemente-Juan, E. Coronado, A. Gaita-Ariño, C. Martí-Gastaldo, F. Luis and O. Montero, Mononuclear lanthanide single molecule magnets based on the polyoxometalates $[Ln(W_5O_{18})_2]^{9-}$ and $[Ln(_2\text{-}SiW_{11}O_{39})_2]^{13-}$(LnIII = Tb, Dy, Ho, Er, Tm, and Yb), *Inorg. Chem.*, 2009, **48**, 3467–3479.

18 X.-L. Li, J. Wu, J. Tang, B. Le Guennic, W. Shi and P. Cheng, A planar triangular $Dy_3 + Dy_3$ single-molecule magnet with a toroidal magnetic moment, *Chem. Commun.*, 2016, **52**, 9570.

19 J. Long, F. Habib, P.-H. Lin, I. Korobkov, G. Enright, L. Ungur, W. Wernsdorfer, L. F. Chibotaru and M. Murugesu, Single-molecule magnet behavior for an antiferromagnetically superexchange-coupled dinuclear dysprosium(III) complex, *J. Am. Chem. Soc.*, 2011, **133**, 5319–5328.

20 J. Wang, C.-Y. Sun, Q. Zheng, D.-Q. Wang, Y.-T. Chen, J.-F. Ju, T.-M. Sun, Y. Cui, Y. Ding and Y.-F. Tang, Lanthanide single–molecule magnets: synthetic strategy, structures, properties and recent advances, *Chem. – Asian J.*, 2023, **18**, e202201297.

21 B. S. Dolinar, D. I. Alexandropoulos, K. R. Vignesh, T. James and K. R. Dunbar, Lanthanide triangles supported by radical bridging ligands, *J. Am. Chem. Soc.*, 2018, **140**, 908–911.

22 S. Bala, M. S. Bishwas, B. Pramanik, S. Khanra, K. M. Fromm, P. Poddar and R. Mondal, Construction of polynuclear lanthanide (Ln = DyIII, TbIII, and NdIII) cage complexes using pyridine–pyrazole-based ligands: versatile molecular topologies and SMM behavior, *Inorg. Chem.*, 2015, **54**, 8197–8206.

23 C.-Y. Jin, X.-L. Mei, Y. Zhou and J.-P. Sutter, Single-molecule magnet behavior in a Tb-nitronyl nitroxide radical network with $[Tb_3(NIT)_2]$ nodes, *Inorg. Chem.*, 2024, **50**, 23829–23836.

24 M. Orts-Arroyo, I. Castro, F. Lloret and J. Martínez-Lillo, Field-induced slow relaxation of magnetisation in two one-dimensional homometallic dysprosium(III) complexes based on alpha-and beta-amino acids, *Dalton Trans.*, 2020, **49**, 9155–9163.

25 S. Benmansour and C. J. Gómez-García, Lanthanoid-anilato complexes and lattices, *Magnetochemistry*, 2020, **6**, 71.

26 S. Benmansour, A. Hernández-Paredes, A. Mondal, G. López Martínez, J. Canet-Ferrer, S. Konar and C. J. Gómez-García, Slow relaxation of the magnetization, reversible solvent exchange and luminescence in 2D anilato-based frameworks, *Chem. Commun.*, 2020, **56**, 9862–9865.

27 S. Benmansour, C. Pintado-Zaldo, J. Martínez-Ponce, A. Hernández-Paredes, A. Valero-Martínez, M. Gómez-Benmansour and C. J. Gómez-García, The Versatility of Ethylene Glycol to Tune the Dimensionality and Magnetic Properties in DyIII-Anilato-Based Single-Ion Magnets, *Cryst. Growth Des.*, 2023, **23**, 1269–1280.

28 P. I. Girginova, L. C. J. Pereira, J. T. Coutinho, I. C. Santos and M. Almeida, Slow magnetic relaxation in lanthanide ladder type coordination polymers, *Dalton Trans.*, 2014, **43**, 1897.

29 J. D. Rinehart and J. R. Long, Exploiting single-ion anisotropy in the design of f-element single-molecule magnets, *Chem. Sci.*, 2011, **2**, 2078–2085.

30 F.-S. Guo, B. M. Day, Y.-C. Chen, M.-L. Tong, A. Mansikkamäki and R. A. Layfield, Magnetic hysteresis up to 80 kelvin in a dysprosium metallocene single-molecule magnet, *Science*, 2018, **362**, 1400–1403.

31 Y.-S. Ding, N. F. Chilton, R. E. P. Winpenny and Y.-Z. Zheng, On approaching the limit of molecular magnetic anisotropy: a near–perfect pentagonal bipyramidal dysprosium(III) single–molecule magnet, *Angew. Chem., Int. Ed.*, 2016, **55**, 16071–16074.

32 Y. Duan, L. E. Rosaleny, J. T. Coutinho, S. Giménez-Santamarina, A. Scheie, J. J. Baldoví, S. Cardona-Serra and A. Gaita-Ariño, Data-driven design of molecular nanomagnets, *Nat. Commun.*, 2022, **13**, 7626.

33 K. Liu, X. Zhang, X. Meng, W. Shi, P. Cheng and A. K. Powell, Constraining the coordination geometries of lanthanide centers and magnetic building blocks in frameworks: a new strategy for molecular nanomagnets, *Chem. Soc. Rev.*, 2016, **45**, 2423.

34 X. Zhang, V. Vieru, X. Feng, J.-L. Liu, Z. Zhang, B. Na, W. Shi, B.-W. Wang, A. K. Powell, L. F. Chibotaru, S. Gao, P. Cheng and J. R. Long, Influence of guest exchange on the magnetization dynamics of dilanthanide single–molecule–magnet nodes within a metal–organic Framework, *Angew. Chem., Int. Ed.*, 2015, **54**, 9861–9865.

35 L.-X. You, B.-B. Zhao, H.-J. Liu, S.-J. Wang, G. Xiong, Y.-K. He, F. Ding, J. J. Joos, P. F. Smet and Y.-G. Sun, 2D and 3D lanthanide metal–organic frameworks constructed from three benzenedicarboxylate ligands: synthesis, structure and luminescent properties, *CrystEngComm*, 2018, **20**, 615–623.

36 Y.-P. Wu, G.-W. Xu, W.-W. Dong, J. Zhao, D.-S. Li, J. Zhang and X. Bu, Anionic lanthanide MOFs as a platform for iron-selective sensing, systematic color tuning, and efficient nanoparticle catalysis, *Inorg. Chem.*, 2017, **56**, 1402–1411.

37 V. Jornet-Mollá and F. M. Romero, Synthesis of rigid ethynyl-bridged polytopic picolinate ligands for MOF applications, *Tetrahedron Lett.*, 2015, **56**, 6120–6122.

38 V. Jornet-Mollá, C. J. Gómez-García, M. J. Dolz-Lozano and F. M. Romero, *Magnetochemistry*, 2025, **11**, 31.

39 V. Jornet-Mollá, C. Dreessen and F. M. Romero, Robust lanthanoid picolinate-based coordination polymers for luminescence and sensing applications, *Inorg. Chem.*, 2021, **60**, 10572–10584.

40 *CrysAlisPro v39.46*, Rigaku Oxford Diffraction Ltd, 2018.

41 L. J. Farrugia, WinGX suite for small-molecule single-crystal crystallography, *J. Appl. Crystallogr.*, 2012, **45**, 849–854.

42 G. M. Sheldrick, Crystal structure refinement with SHELXL, *Acta Crystallogr., Sect. C:Struct. Chem.*, 2015, **71**, 3–8.

43 G. A. Bain and J. F. Berry, Diamagnetic corrections and Pascal's constants, *J. Chem. Educ.*, 2008, **85**, 532–536.

44 A. C. Sudik, A. R. Millward, N. W. Ockwig, A. P. Côté, J. Kim and O. M. Yaghi, Design, synthesis, structure, and gas (N_2, Ar, CO_2, CH_4, and H_2) sorption properties of porous metal-organic tetrahedral and heterocuboidal polyhedral, *J. Am. Chem. Soc.*, 2005, **127**, 7110–7118.

45 M.-L. Han, G.-W. Xu, D.-S. Li, L. M. Azofra, J. Zhao, B. Chen and C. Sun, A terbium–organic framework material for highly sensitive sensing of Fe^{3+} in aqueous and biological systems: experimental studies and theoretical analysis, *ChemistrySelect*, 2016, **1**, 3555–3561.

46 D. Casanova, P. Alemany, J. M. Bofill and S. Alvarez, Shape and symmetry of heptacoordinate transition–metal complexes: structural trends, *Chem. – Eur. J.*, 2003, **9**, 1281–1295.

47 S. Alvarez, P. Alemany, D. Casanova, J. Cirera, M. Llunell and D. Avnir, Shape maps and polyhedral interconversion paths in transition metal chemistry, *Coord. Chem. Rev.*, 2005, **249**, 1693–1708.

48 M. Llunell, D. Casanova, J. Cirera, J. M. Bofill, P. Alemany and S. Alvarez, *SHAPE (Version 2.1)*, Barcelona, 2013.

49 S. Alvarez, D. Avnir, M. Llunell and M. Pinsky, Continuous symmetry maps and shape classification. The case of six-coordinated metal compounds, *New J. Chem.*, 2002, **26**, 996–1009.

50 A. L. Spek, Single-crystal structure validation with the program PLATON, *J. Appl. Crystallogr.*, 2003, **36**, 7–13.

51 K. Akhbari and A. Morsali, Modulating methane storage in anionic nano-porous MOF materials via post-synthetic cation exchange process, *Dalton Trans.*, 2013, **42**, 4786–4789.

52 M. Mon, E. Tiburcio, J. Ferrando-Soria, R. G. S. Millán, J. A. R. Navarro, D. Armentano and E. Pardo, A post-synthetic approach triggers selective and reversible sulphur dioxide adsorption on a metal–organic framework, *Chem. Commun.*, 2018, **54**, 9063–9066.

53 J. Xia, B. Zhao, H.-S. Wang, W. Shi, Y. Ma, H.-B. Song, P. Cheng, D.-Z. Liao and S.-P. Yan, Two- and three-dimensional lanthanide complexes: synthesis, crystal structures, and properties, *Inorg. Chem.*, 2007, **46**, 3450–3458.

54 L. Sorace and D. Gatteschi, Electronic Structure and Magnetic Properties of Lanthanide Molecular Complexes, in *Lanthanides and Actinides in Molecular Magnetism*, Wiley-VCH, 2015, pp. 1–26.

55 J. W. de Oliveira Maciel, M. A. Lemes, A. K. Valdo, R. Rabelo, F. T. Martins, L. J. Queiroz Maia, R. C. de Santana, F. Lloret, M. Julve and D. Cangussu, *Inorg. Chem.*, 2021, **60**, 6176–6190.

56 K. E. Vostrikova, T. S. Sukhikh and A. N. Lavrov, The Synthesis, Crystal Structure, and Magnetic Properties of Mono-Scorpionate Eu(III) Complexes, *Inorganics*, 2023, **11**, 418.

57 S. Benmansour, C. Cerezo-Navarrete and C. J. Gómez-García, Slow Relaxation of the Magnetisation in a Two-Dimensional Metal–Organic Framework with a Layered Square Lattice, *Magnetochemistry*, 2025, **11**, 1.

58 P. Kalita, A. Malakar, J. Goura, S. Nayak, J. M. Herrera, E. Colacio and V. Chandrasekhar, Europium(III), terbium (III), and gadolinium(III) oxamato-based coordination polymers: visible luminescence and slow magnetic relaxation, *Dalton Trans.*, 2019, **48**, 4857.

59 N. F. Chilton, R. P. Anderson, L. D. Turner, A. Soncini and K. S. Murray, PHI: A powerful new program for the analysis of anisotropic monomeric and exchange-coupled poly-nuclear *d*- and *f*-block complexes, *J. Comput. Chem.*, 2013, **34**, 1164–1175.

60 R. J. Blagg, L. Ungur, F. Tuna, J. Speak, P. Comar, D. Collison, W. Wernsdorfer, E. J. L. McInnes, L. Chibotaru and R. E. P. Winpenny, Magnetic relaxation pathways in lanthanide single-molecule magnets, *Nat. Chem.*, 2013, **5**, 673–678.

61 M.-H. Wang, M.-Y. Tsai, Y.-C. Su, S.-T. Chiu, P.-H. Lin and J. Long, Zero-field single-molecule magnet behavior in a series of dinuclear dysprosium(III) complexes based on benzothiazolyl-based ligands and (-diketonates, *Cryst. Growth Des.*, 2024, **24**, 422–431.

62 S. Demir, J. M. Zadrozny and J. R. Long, Large spin–relaxation barriers for the low–symmetry organolanthanide complexes [Cp*$_2$Ln(BPh$_4$)] (Cp*=pentamethylcyclopentadienyl; Ln=Tb, Dy), *Chem. – Eur. J.*, 2014, **20**, 9524–9529.

63 Z. Zhu, M. Guo, X. Li and J. Tang, Molecular magnetism of lanthanide: advances and perspectives, *Coord. Chem. Rev.*, 2019, **378**, 350–364.

64 V. S. Parmar, D. P. Mills and R. E. P. Winpenny, Mononuclear dysprosium alkoxide and aryloxide single–molecule magnets, *Chem. – Eur. J.*, 2021, **27**, 7625–7645.

65 A. Zabala-Lekuona, J. M. Seco and E. Colacio, Single-molecule magnets: from Mn$_{12}$-ac to dysprosium metallocenes, a travel in time, *Coord. Chem. Rev.*, 2021, **441**, 213984.

66 T. G. Ashebr, H. Li, X. Ying, X.-L. Li, C. Zhao, S. Liu and J. Tang, Emerging trends on designing high-performance dysprosium(III) single-molecule magnets, *ACS Mater. Lett.*, 2022, **4**, 307–319.

67 M. Orendáč, L. Sedláková, E. Čizmár, A. Orendáčova, A. Feher, S. A. Zvyagin, J. Wosnitza, W. H. Zhu, Z. M. Wang and S. Gao, Spin relaxation and resonant phonon trapping in [Gd$_2$(fum)$_3$(H$_2$O)$_4$]·3H$_2$O, *Phys. Rev. B:Condens. Matter Mater. Phys.*, 2010, **81**, 214410.

68 A. Rossin, G. Giambastiani, M. Peruzzini and R. Sessoli, Amine-templated polymeric lanthanide formates: synthesis, characterization, and applications in luminescence and magnetism, *Inorg. Chem.*, 2012, **51**, 6962–6968.

69 M. Orts-Arroyo, R. Rabelo, A. Carrasco-Berlanga, N. Moliner, J. Cano, M. Julve, F. Lloret, G. De Munno, R. Ruiz-García, J. Mayans, J. Martínez-Lillo and I. Castro, *Dalton Trans.*, 2021, **50**, 3801–3805.

70 M. Orts-Arroyo, A. Sanchis-Perucho, N. Moliner, I. Castro, F. Lloret and J. Martínez-Lillo, *Inorganics*, 2022, **10**, 32.

71 Y. C. Chen, Y.-Y. Peng, J.-L. Liu and M.-L. Tong, *Inorg. Chem. Commun.*, 2019, **107**, 107449.

72 J. Mayans and A. Escuer, *Chem. Commun.*, 2021, **57**, 721–724.

73 (a) V. Jornet-Mollá, C. J. Gómez-García, M. J. Dolz-Lozano, C. Giménez-Saiz and F. M. Romero, CCDC 2392560: Experimental Crystal Structure Determination, 2025, DOI: 10.5517/ccdc.csd.cc2l9ncy; (b) V. Jornet-Mollá, C. J. Gómez-García, M. J. Dolz-Lozano, C. Giménez-Saiz and F. M. Romero, CCDC 2392561: Experimental Crystal Structure Determination, 2025, DOI: 10.5517/ccdc.csd.cc2l9ndz; (c) V. Jornet-Mollá, C. J. Gómez-García, M. J. Dolz-Lozano, C. Giménez-Saiz and F. M. Romero, CCDC 2392562: Experimental Crystal Structure Determination, 2025, DOI: 10.5517/ccdc.csd.cc2l9nf0; (d) V. Jornet-Mollá, C. J. Gómez-García, M. J. Dolz-Lozano, C. Giménez-Saiz and F. M. Romero, CCDC 2392563: Experimental Crystal Structure Determination, 2025, DOI: 10.5517/ccdc.csd.cc2l9ng1; (e) V. Jornet-Mollá, C. J. Gómez-García, M. J. Dolz-Lozano, C. Giménez-Saiz and F. M. Romero, 2025, CCDC 2392564: Experimental Crystal Structure Determination, DOI: 10.5517/ccdc.csd.cc2l9nh2.